

# Bond coat assisted enhancement in microstructural, mechanical and corrosion behavior of AZ91 magnesium alloy cold spray coated with aluminum alloys



Sridhar Niverty<sup>a,\*</sup>, Rajib Kalsar<sup>a</sup>, Anthony J. Naccarelli<sup>b</sup>, Timothy J. Eden<sup>b</sup>, Xiaolong Ma<sup>a</sup>, Nicole Overman<sup>a</sup>, Glenn Grant<sup>a</sup>, Darrell Herling<sup>a</sup>, Vineet V. Joshi<sup>a,\*</sup>

<sup>a</sup> Energy and Environment Directorate, Pacific Northwest National Laboratory, 902 Battelle Boulevard, Richland, WA 99354, USA

<sup>b</sup> Engineering Science and Mechanics Department, Pennsylvania State University, State College, PA 16801, USA

## ARTICLE INFO

### Keywords:

Cold spray  
Coatings  
Magnesium alloys  
Mechanical behavior  
Solid phase processing  
Scanning electrochemical cell microscopy  
Multimodal corrosion

## ABSTRACT

Cold spray coating technique was used to deposit coatings of AA6061 aluminum alloy on AZ91 magnesium alloy substrates. A bond coat of commercially pure aluminum was used to facilitate deposition of the AA6061 powders. Two cold spray coating iterations were conducted to optimize the coating's microstructural features such as porosity, surface roughness, and interface microstructure. Mechanical properties such as hardness, wear resistance, and adhesion behavior were characterized and used as metrics to compare the coatings with the substrate. The corrosion behavior of the coated and uncoated samples was characterized using multiscale and multimodal corrosion measurements comprising macroscopic potentiodynamic polarization and scanning electrochemical cell microscopy. The coated substrates exhibited a significant improvement in mechanical and corrosion performance as compared to the uncoated substrate.

## 1. Introduction

The use of magnesium (Mg) and its alloys has been steadily increasing in automotive applications. Mg alloys exhibit a high specific strength and enable weight savings of 30–70 % in automobile components [1–3]. However, their poor corrosion performance is responsible for their limited implementation in automotive and aerospace applications. These alloys are often exposed to harsh corrosive environments such as exposure to salt and muddy water, moisture and dry-wet cycling during service [4]. Furthermore, as a part of multimaterial joints, their use with aluminum (Al) alloys and steels leads to significant galvanic corrosion [3–6].

Coating methods have the potential for offering excellent surface protection against corrosive environments. Methods for corrosion protection of automotive Mg alloys such as micro-arc oxidation, ceramic powder coating etc., are widely used by the original equipment manufacturers [7]. However, these coatings are very thin (<10 μm), porous, and are susceptible to cracking under service conditions that often involve the combination of corrosive environments and mechanical stresses. The corrosive environments these vehicle components are

exposed often lead to corrosive solution ingress to the Mg substrate, leading to the initiation and propagation of localized and general corrosion damage [8,9]. Thus, there is a need to develop a coating technique that meets several material and process requirements; namely, negligible porosity to prevent corrosive solution ingress to the substrate, wear and corrosion properties comparable to the material that the coated Mg alloy will be coupled with, and finally, the technique must be scalable into automotive production lines and the coating must be easily recyclable (i.e., without placing extra burden on the material's end of life recycling processes).

Cold spray technology meets these requirements. It offers distinct advantages to the surface protection of light metal alloys such as Al and Mg alloys over existing methods. Cold spray is a solid phase coating technique in which powders of the coating material are impacted onto surfaces at supersonic velocities, leading to formation of a layer coat. The use of a relatively low temperature (i.e., below the melting points of the coating and substrate materials) gas to impinge the powders onto the substrate causes minimal intermetallic formation during deposition and leads to the formation of a coating and substrate region with tunable residual stress distribution to benefit fatigue performance [10].

\* Corresponding authors.

E-mail addresses: [sridhar.niverty@pnnl.gov](mailto:sridhar.niverty@pnnl.gov) (S. Niverty), [Vineet.joshi@pnnl.gov](mailto:Vineet.joshi@pnnl.gov) (V.V. Joshi).

Furthermore, the combination of high pressures and temperatures, which through gas expansion result in particle velocity, can facilitate the formation of a metallurgical bond between the coating and the substrate, which in turn leads to a high adhesion strength [11–13]. Cold spray offers the advantage of being scalable and facilitates the selective coating of specific regions in complex geometries. This technique is also employed to swiftly and economically repair and recoat damaged surfaces or parts [14]. With the correct choice of coating material, Mg alloy components can be successfully coupled with parts with dissimilar compositions (such as other Al alloys or steels) in automotive components to greatly reduce or eliminate galvanic coupling.

An example of an alloy of interest for coupling with Mg alloys in service is Al alloy AA6061. A coating of AA6061 on Mg alloys has proven to be very beneficial in eliminating differences in corrosion and wear behaviors. Few studies have investigated the microstructure, corrosion, and mechanical properties of Mg alloys cold-spray coated with commercially pure Al (CP-Al) and AA6061. These coatings have shown promise to improve surface properties such as wear rate and corrosion behavior compared to the uncoated Mg alloy substrates [15–18]. However, the challenges associated with depositing Al alloys on to Mg alloy substrates are not new. At low carrier gas temperatures, it is

observed that the coating can be porous (greater than 1 %) and deposition rates can be low. These problems usually are overcome by the addition of harder particles such as alumina to form a metal matrix composite as a coating or by using heavier and larger particles to peen the smaller coating powders to the substrate without adhering to the substrate itself [19,20]. However, these methods increase cold spray costs and lead to additional cleaning and separation steps during end-of-life recycling. Thus, to enable better deposition density, increase deposition efficiency, and reduce cost, it is worth exploring the cold spray temperature/pressure parameter landscape and investigating the use of higher pressures and temperatures to optimize deposition and reduce coating porosity [21–23]. Furthermore, understanding the metallurgical bond and the factors that affect it at the substrate-coating interface is essential as it dictates in part the adhesion performance of the coating. Finally, reduced porosity and greater deposition thickness also ensures better corrosion performance and prevents the corrosive fluid from reaching the substrate. Multiple strategies can be explored to achieve overall greater deposition efficiency. In this study, we explored the use of a combination of high carrier gas temperature and pressure. Additionally, we also explored the use of a bond coating to improve bonding and deposition.

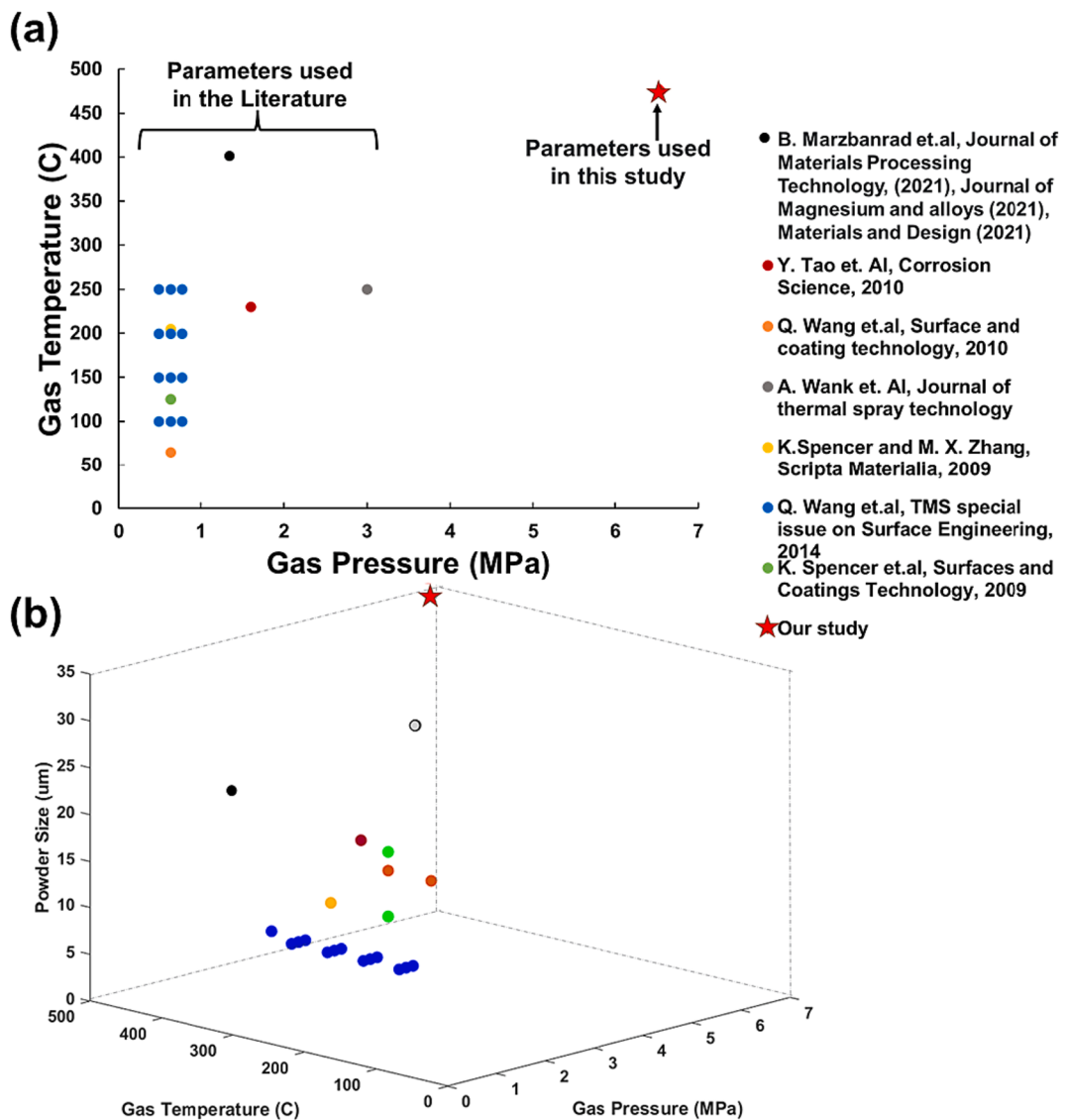


**Fig. 1.** Comparison of cold spray process parameters used in the literature [10,15–18,24–27] vs. those used in the current study. (a) Two-dimensional plot showing carrier gas temperature and pressure, and (b) three-dimensional plot showing carrier gas temperature, pressure and average powder particle size used.

In this study, we report cold spray process improvements in the deposition of a coating of AA6061 Al alloy on AZ91 Mg alloy. Fig. 1 shows a comparison of the cold spray coating parameters namely gas temperature, gas pressure, and powder size documented in the literature in comparison to the parameters used in this study for depositing Al onto Mg substrates. We used a higher temperature, pressure, and powder size to enable improved deposition of the powders onto the substrate [10,15–18,24–27]. Through a sequential series of coating strategies (two of which are described in this manuscript) and accompanying coating performance evaluation and microstructural analysis, we have compared three cases: 1) uncoated AZ91 coupons, 2) AZ91 coupons coated with only AA6061 powders, and 3) AZ91 coupons coated with an optimized bond coat of CP-Al and a top coat of AA6061. The coatings were comprehensively characterized and evaluated based on their microstructure (i.e., porosity, roughness, and coating thickness) and mechanical behavior (i.e., hardness and adhesion strength). Multiscale corrosion testing using a multimodal corrosion measurement setup (simultaneous sample imaging and electrochemical testing involving open circuit potential [OCP] and potentiodynamic [PD] polarization) and localized scanning electrochemical cell microscopy (SECCM) were performed to compare the corrosion behaviors of the coating to the substrate and to study the role of coating in protecting the substrate from corrosion [28–30]. Finally, we present the implications of these properties on the coating performance and compare it to that reported in the literature to understand opportunities for further process control.

## 2. Experimental methods

Several iterations of cold spray coatings (two of which are discussed in this manuscript) were performed as a part of this study to document the improvement of coating microstructure and mechanical and corrosion performance. In this manuscript, coatings with two different conditions are discussed, namely Case-I and Case-II. Fig. 2 shows a schematic of the two coatings discussed in this manuscript. A VRC Metal Systems Gen III High-Pressure Cold Spray System with a converging-diverging De Laval PBI nozzle (NZZL0070) was used. Nitrogen ( $N_2$ ) gas was used as carrier gas to accelerate Al particles to supersonic velocities to adhere the particles onto the Mg-substrate. The current cold spray process parameters are shown in Table 1. Powders of AA6061 were procured from Solvus Global (Worcester, MA) and were used as-received (neither sieved, nor heat treated). To improve the deposition quality of AA6061, CP-Al was used as a bond coat for the Case-II sprays. The CP-Al powders were procured from Valimet (H-15 powders) and were sieved (+20  $\mu\text{m}$ /-53  $\mu\text{m}$ ) and annealed (220–240 °C in argon for 1 h) prior to being cold sprayed. For both the cases, the powder feeder was set at 6 rpm (powder mass feed rate was assumed constant) and spray distance was 25.4 mm. A single 45-degree pass was used in the Case-I-AA6061 bonding to the substrate and in Case-II, a layer of CP-Al coating was applied to promote adhesion of particles on to the substrate. Following the initial layer, 10 passes were sprayed at 90° deposition

**Table 1**

Process parameters and estimated particles velocities for each of the two cold spray coatings.

	Case I	Case II
Substrate	AZ91D	AZ91D
Bond coat	No	Yes
Gas pressure (MPa)	6.5	6.5
Gas Temperature (°C)	425	375 (CP-Al); 425 (AA6061)
Powder feed rate (RPM)	6	6
Spray distance (mm)	25.4	25.4
Cold spray gas	Nitrogen	Nitrogen
Spray angle	1 pass at 45° spray angle and 5 passes at 90° spray angle	CP-Al: 1 pass at 45° spray angle and 5 passes at 90° spray angle AA6061: 5 passes at 90° spray angle
Estimated particle velocity at impact (m/s)	20 $\mu\text{m}$ – 725 53 $\mu\text{m}$ – 628	CP-Al 20 $\mu\text{m}$ – 725 CP-Al 53 $\mu\text{m}$ – 628 AA6061 20 $\mu\text{m}$ – 749 AA6061 53 $\mu\text{m}$ – 643
Estimated critical velocity (m/s)	20 $\mu\text{m}$ – 471 53 $\mu\text{m}$ – 438	CP-Al 20 $\mu\text{m}$ – 471 CP-Al 53 $\mu\text{m}$ – 438 AA6061 20 $\mu\text{m}$ – 651 AA6061 53 $\mu\text{m}$ – 590

angle to the substrate. Commercially available AZ91D Mg plates produced by high pressure die casting were provided by Meridian Lightweight Technologies (Ontario, CA). Flat AZ91 coupons with dimensions of 50.8 mm x 50.8 mm x 3.0 mm were coated. The coupon substrates were roughened with green scotch brite and cleaned with ethanol before cold spray coating. A substrate surface roughness of 0.4–1.0  $\mu\text{m}$  Ra was measured with a Taylor Hobson Sutronic S128 stylus profilometer prior to spraying.

Cold spray coatings are created through high-velocity impacts between particles and a substrate or previously deposited powder materials. As the bonding event is driven by the kinetic energy of the particles, a model for the critical velocity needed to create a bond in cold spray is used widely throughout the community as an estimate for whether or not bonding will occur. Estimated critical velocities for CP-Al and AA6061 particles with sizes of 20 and 53  $\mu\text{m}$  were calculated using an empirical equation given by Schmidt et al. [22,31]. The critical velocity of a particle given as:

$$V_{cr} = \sqrt{\frac{4\sigma_u(1 - \theta)}{\rho_p} + 0.25c_p(T_m - T_i)}$$

where,  $\sigma_u$ ,  $\rho_p$ ,  $T_m$ ,  $T_p$ ,  $T_i$  and  $c_p$  are the ultimate strength, density, melting temperature, reference temperature for mechanical properties (293 K), impact temperature and specific heat.

$$\theta = \frac{T_i - TR}{T_m - TR}$$

(a) Case I



(b) Case II

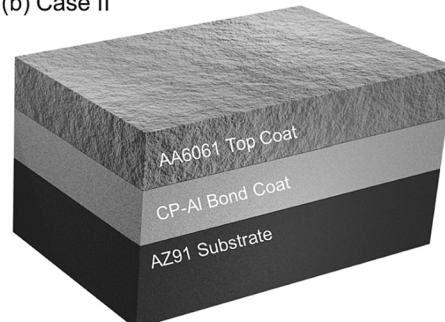


**Fig. 2.** (a) Case -I, AA6061 directly coated on top of AZ91 substrate and (b) Case -II, CP-Al coated as bond coat and AA6061 coated on top of AZ91 substrate.

**Table 2** shows the materials parameters for Al and AA6061 used for critical velocity calculations.

Following the cold spray coating process, the samples were sectioned, and their cross sections mounted and polished down to a 50 nm colloidal silica finish. Scanning electron microscopy (SEM) (JEOL IT500) was used to investigate microstructural features such as deformed particle morphology, porosity, interparticle oxides from the cross sections of the substrate, coating layers, and the interfaces. Energy dispersive X-ray spectroscopy (EDS) was performed at 20 kV (Oxford detector and INCA microanalysis software) at a magnification of 5000 $\times$  to study elemental segregation and oxide formation. Furthermore, electron back-scattered diffraction (EBSD) analysis was performed using a JEOL JSM-7600F field emission SEM, equipped with Oxford Instruments and Aztec NanoAnalysis software package. EBSD data analysis was performed using Channel5 HKL software. Location-specific transmission electron microscopy (TEM) samples were prepared using a Ga<sup>+</sup> focused ion beam. TEM analyses were performed on the cross section of the coated samples using an aberration corrected electron microscope, (JEM-ARM200CF from JEOL, Japan) equipped with high angle annular dark field (HAADF) detectors and an EDS system operated at 200 kV for bright field, selected area diffraction pattern, HAADF and high-resolution TEM and compositional analysis.

The mechanical behavior of the coatings was characterized using a Vickers Microhardness tester (CM-700AT Sun-Tec Corporation) to estimate the hardness of the individual coating layers on the samples from each case. Because the coating ideally would be in contact with an Al alloy in service, it is essential to make sure the coating does not wear out preferentially via abrasion. Wear tests were conducted on the optimized coating and compared to the uncoated AZ91. An Anton Paar Pin-on-disk tribometer was utilized to perform wear test in accordance with ASTM G-133. A 6 mm diameter tungsten carbide (WC) ball was used as a counterpart. Wear tests were conducted under a normal load of 1 N over 5000cycles (sliding frequency 5 Hz) for a sliding distance of 120 m with a stroke length of 6 mm. Three replicates were performed for each sample and all tests were performed in ambient air. Tribo 1.4x software was used to record the coefficient of friction (COF) and the wear tracks were analyzed using a Keyence white light interferometer. 3D profiles of the wear tracks were measured and analyzed to calculate the wear volume loss ( $\text{mm}^3$ ) using VR-5000 series software. Wear rates ( $\text{mm}^3/\text{N.m}$ ) were calculated by dividing wear volume loss by normal load and the sliding distance. Furthermore, adhesion tests were conducted per ASTM Standard D4541 to obtain coating adhesion strength values for each case. Solvay FM1000 was the epoxy used for adhesion testing. A DeFelsko PosiTTest AT was used to complete adhesion testing. Failure analysis was conducted on these samples to understand the mechanisms leading to the failure of the coatings and were further correlated with microstructure.

The corrosion behavior of both the coatings in comparison with uncoated AZ91 was investigated using a newly developed multimodal corrosion system capable of acquiring corrosion parameters (current and voltage) and performing sample imaging to capture ongoing changes to sample surface during the corrosion process. The samples (uncoated AZ91, a coated sample from Case-I, and a coated sample from Case-II) were polished to a 1  $\mu\text{m}$  diamond finish. A Gamry G750 potentiostat was used alongside a saturated calomel electrode (SCE) as a reference electrode and graphite rods as counter electrodes. Further details about

**Table 2**  
Material properties for particles.

Material	Al	AA6061
Density ( $\text{kg}/\text{m}^3$ )	2700	2700
Heat Capacity ( $\text{J}/(\text{kg}\cdot\text{K})$ )	900	896
Melt Temperature (K)	933	855
Thermal Conductivity ( $\text{W}/(\text{m}\cdot\text{K})$ )	247	167
Ultimate Tensile Strength (MPa)	90	310

the multimodal corrosion system can be found in references [28,32]. In each case, an OCP estimation was performed for a duration of 1,800 s (30 min) after which PD polarization was performed from an applied potential of 200 mV below the estimated OCP, up to a potential of  $\sim 800$  mV above the estimated OCP. Images of the samples during the electrochemical measurements also are included to show the difference in the nature of corrosion attack for each material.

SECCM was used to study microscopic electrochemical behavior of coating and substrate. We used an SECCM platform purchased from HEKA (PG618 USB double amplifier) to measure electrochemical properties of substrate and coating. A theta capillary made of borosilicate glass with  $\sim 10 \mu\text{m}$  in diameter was used for microscopic electrochemical properties. We used a diluted solution with 0.01 M sodium chloride (NaCl) as the electrolyte. A 0.25 mm diameter silver/silver chloride (Ag/AgCl) wire was used as a quasi-reference electrode, and a 0.25 mm diameter platinum wire was used as a counter electrode. Details of the measurement method can be found in reference [30].

### 3. Results

#### 3.1. Microstructure: CP-Al and AA6061 powders

Figs. 3(a-b) show the morphology of CP-Al powder particles obtained using SEM and their cross-sectioned microstructures obtained using EBSD, respectively. Particles are spherical in shape with most of the particles containing multiple grains per particle (average grain size:  $44.6 \pm 10 \mu\text{m}$ ). Fig. 3 (c) shows the presence of oxide ( $\text{Al}_2\text{O}_3$ ) layer at outer surface of each CP-Al powder. The average oxide layer was  $3.7 \pm 0.3$  nm. Similarly, Fig. 3(d) and 3(e) show the morphology of AA6061 powder particles obtained using SEM and their cross-sectioned microstructures obtained using EBSD, respectively. Fig. 3(e) shows the presence of a  $5.3 \pm 1.0$  nm oxide layer at the outer surface of each AA6061 powder, as has been observed in other studies [33]. TEM-EDS maps showing the presence of the  $\text{Al}_2\text{O}_3$  layer are included as Fig. S1 in the supplementary section. Furthermore, these powders also contain relatively large grains (average grain size:  $45.5 \pm 8.1 \mu\text{m}$ ) within each particle.

#### 3.2. Microstructure: Coated samples

Fig. 4 shows images from the cross section of a sample coated using the parameters stated in Case 1. Fig. 4(a) shows a back scattered SEM image of the coating and substrate showing the presence of pores in the microstructure (blue arrows). The coating also is absent in certain portions as seen by the crater (yellow arrow). Figs. 4(b), (c) and (d) show high resolution images of the coating, interface region and substrate. The coating consists of interparticle porosity and oxides (Fig. 4(b)). The substrate immediately below the interface is deformed due to the supersonic impact of the cold sprayed particles (Fig. 4(c)) with the deformation visible until  $\sim 30 \mu\text{m}$  from the interface. The substrate consists of a combination of black porosity, dark Mg matrix, light grey  $\text{Mg}_{17}\text{Al}_{12}$  and bright Al-Mn rich particles (Fig. 4(d)). Fig. 4(e) shows a SEM microstructure and corresponding EDS maps of the region marked in green box in Fig. 4(b) showing the presence of porosity and interparticle oxide at the interface. Fig. 4(f) shows the SEM microstructure and corresponding EDS maps of interface region. SEM microstructure shows interparticle void and EDS maps shows presence of oxide layer at interparticle region. EDS maps of substrate material is shown in Fig. 4(g). EDS data indicate presence of eutectic  $\beta$ -phase ( $\text{Mg}_{17}\text{Al}_{12}$ ) in Mg-rich matrix [34–36].

Fig. 5 shows a cross section from a Case-II sample coated with optimized coating parameters (i.e., with an CP-Al bond coat and AA6061 top coat). Compared to Case-I (Fig. 4), Case II has a drastic decrease in porosity as shown in Table 3. Additionally, the roughness of the layers is seen to decrease significantly as well. Fig. 5(a) shows a montage captured using back-scatter imaging of the substrate, bond

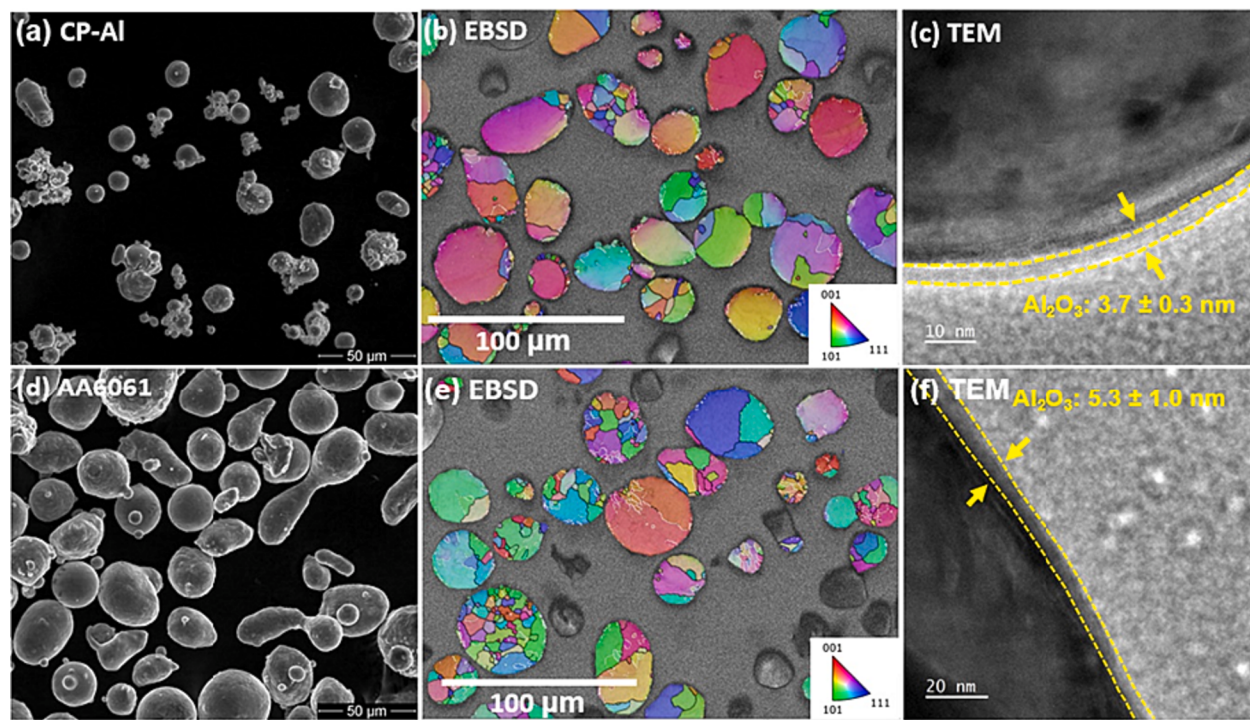


**Fig. 3.** (a), (b) SEM and EBSD microstructures of CP-Al powders. (c) TEM microstructure showing native oxide layer on a CP-Al powder particle, (d), (e) SEM and EBSD microstructures of AA6061 powder. (f) TEM microstructure showing native oxide layer on a AA6061 powder.

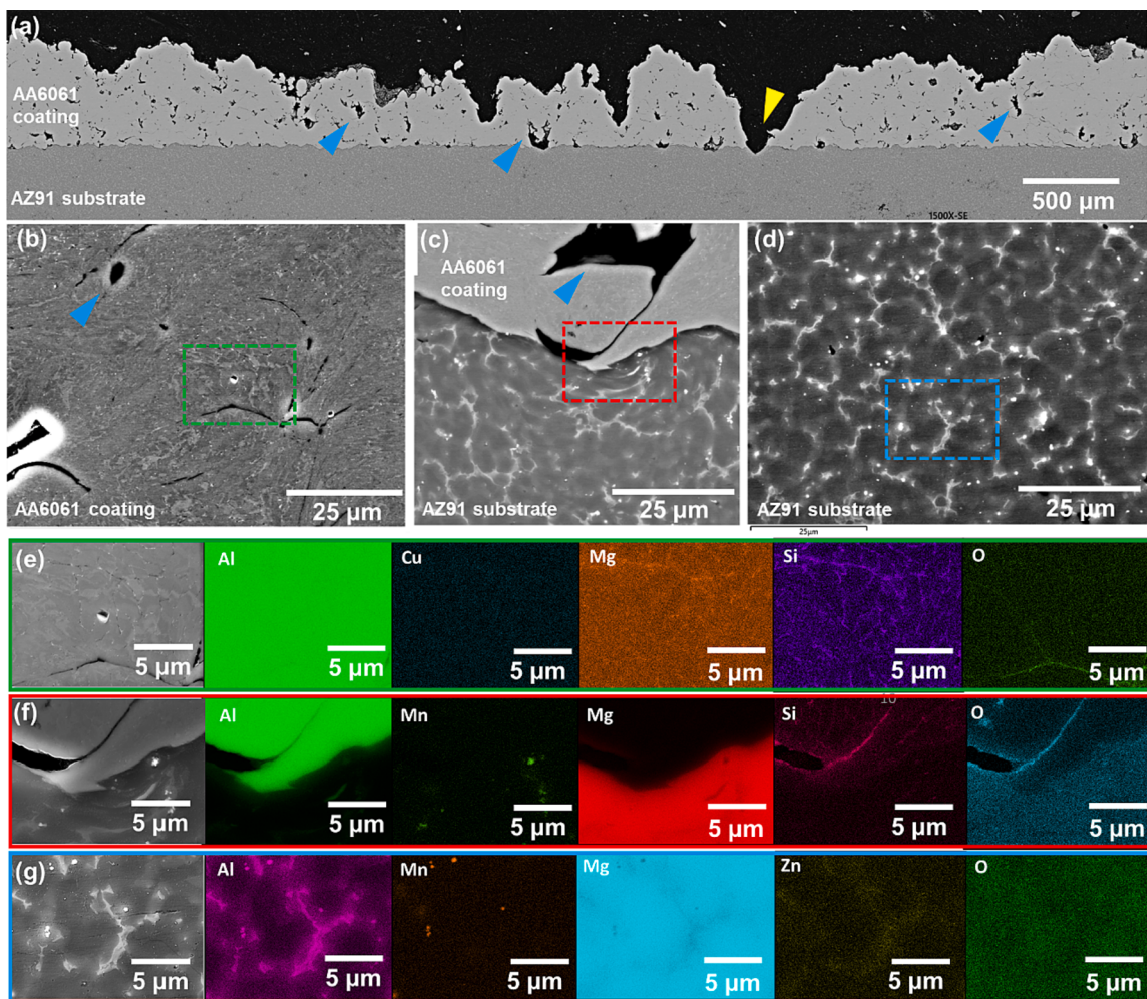
coating, and top coating. Fig. 5(b) shows high resolution images of the top coating layer, topcoat-bond coat interface, bond coating layer, bond coat-substrate interface, and substrate layer. Correspondingly, EDS maps from the top coat-bond coat interface and bond coat–substrate interface are shown in Fig. 5(c) and 5(d).

Fig. 6(a) shows a schematic of the cross section of an AZ91 sample coating under Case-II conditions. Highlighted are three regions namely region 1 (AA6061–Al interface), region 2 (Al–AZ91 substrate interface), and region 3 (within substrate). Also included are the band contrast maps of the regions where EBSD maps were obtained. Upon cold spraying onto the AZ91 substrate, the particles undergo significant deformation and form pancake shaped grains as shown in Fig. 6(b). Its corresponding kernel average misorientation (KAM) map shows a higher degree of localized strain accumulation (green pixels) in the AA6061 coating as compared to Al bond coat layer (Fig. 6(c)). In Fig. 6(e), the diffraction signal obtained from the substrate near the interface was not indexable due to high strain accumulation and hence is shown in black pixels. The grain structure within the coating Al coating is similar to that seen in Fig. 6(b). The interior of particles primarily consists of large grains, while the boundaries of these particles are decorated with small grains (<5 µm) that form due to deformation induced dynamic recrystallization of small grains. The region of the matrix showing strain accumulation due to particles imping on the surface is observed to be 30 ± 5 µm below the Al–AZ91 interface. Fig. 6(g) and 6(h) show the grain structure within the AZ91 substrate unaffected by the cold spray process.

To investigate the metallurgical bond formation between the coating and substrate, we used STEM imaging to characterize the formation of phases at the coating-substrate interface. Fig. 7 shows a STEM image and elemental distribution maps at the substrate and coating (AA6061) interface for a Case-I sample. The yellow line indicates an interface between the AZ91 substrate and the AA6061 coating. Fig. 7(a) shows the presence of pores and inter-particle voids. Fig. 7(b) shows the EDS elemental map highlighting Al, Mg, oxygen, silicon (Si), and zinc (Zn) elements. EDS map shows the presence of Mg-oxide at interface and inter-particle voids. At the inter-particle voids,  $\text{Al}_2\text{O}_3$  is also observed.

The native surface oxide in precursor powders could be the primary source of oxygen in these inter-particle regions. Mg- and Si-rich precipitates also are observed along the interface. Additionally, Zn enrichment also is noticed along interface. Hengyong et al. showed formation of  $\text{Mg}_{17}\text{Al}_{12}$  phase in post-heat-treated interface of cold sprayed Al on AZ91D substrate, while Qiang et al. also showed intermixing of Al and Mg at the interface due to local temperature increases that could facilitate atomic diffusion across the interface [17,37]. Fig. 7(c) and (d) show the EDS line scan across the interface showing elemental distribution of Mg, Al, and oxygen. The line scan data indicates presence of Al-Mg phase ( $\text{Mg}_{17}\text{Al}_{12}$ ) and  $\text{MgO}$  layer at the interface. The thickness of the  $\text{Mg}_{17}\text{Al}_{12}$  phase and  $\text{MgO}$  regions is approximately 80 nm and 60 nm, respectively.

Fig. 8 shows the interface TEM microstructure in the Case-II sample. Fig. 8(a), (b) show the microstructure and elemental distribution at the AA6061 and CP-Al interface region. The microstructure shows a pancaked grain structure within the AA6061 coating and an equiaxed structure in the CP-Al side. The microstructure also shows grain size at interface region is in sub-micron range for both coating sides. To understand the elemental distribution at the interface region, we performed TEM EDS analysis (Fig. 8 (b)). The EDS data indicate the presence of approximately 30 nm thick oxide layer at the CP-Al–AA6061 interface. The presence of a Si-rich phase on the AA6061 side could indicate the presence of  $\text{Mg}_2\text{Si}$  as an alloy. However, on the CP-Al side, no other elemental segregation was observed. Fig. 8(c) and (d) shows the TEM microstructure and EDS image of the CP-Al and AZ91 interface regions. The microstructure shows a sub-micron sized elongated grain structure on the CP-Al side (average grain size ~ 350 nm) and a nano-crystalline structure on the Mg side. The micron-sized grain structure in the Mg substrate region shows a nanocrystalline (average grain size ~ 84 nm) microstructure due to significant deformation induced recrystallization caused by the impact of CP-Al particles during coating. The EDS map shows the presence of a thin oxide layer (~15 nm) at the CP-Al–AZ91 interface (Fig. 8d). To understand the inter-diffusion of elements between the coating-bondcoat and bondcoat–AZ91 substrate, we performed TEM EDS line scan analysis. The EDS line scan data



**Fig. 4.** SEM analysis of the cross section of a specimen from Case-I. (a) Montage showing the deposited AA6061 coating on AZ91 substrate. (b) High-resolution micrograph of the AA6061 coating. (c) High-resolution micrograph of the interface between the AA6061 coating and AZ91 substrate. (d) High-resolution micrograph of the AZ91 substrate. (e) SEM and EDS composition maps showing region (dashed red box in (b)) in the coating. (f) SEM and EDS composition maps showing region (dashed red box in (c)) at the coating-substrate interface. (g) SEM and EDS composition maps showing region (dashed blue box in (d)) in the substrate. (For interpretation of the references to colour in this figure legend, the reader is referred to the web version of this article.)

show the presence of a very thin Al-oxide layer (~20 nm) at both interfaces (Fig. 9). The data indicate no inter-diffusion of elements takes place between the AA6061 top coat-CP-Al bondcoat and the CP-Al bondcoat-AZ91 substrate. The HRTEM images of various phases, along with their corresponding FFT analyses for phase identification are provided in Fig. S2 in the supplementary section.

### 3.3. Mechanical performance

Vickers microhardness line measurements were performed on the cross section of the cold-sprayed samples, from substrate to coating with a step size of 0.25 mm. Measurements were performed along three lines across the interface. Fig. 10 shows the hardness profiles for Case-I and Case-II coatings. In Case-I, the average hardness of the substrate and coating were 73 and 74 HV, respectively. A high variation of hardness was observed within the cast AZ91 alloy substrate due to microstructural inhomogeneity caused by the presence of eutectic  $\beta$ -Mg<sub>17</sub>Al<sub>2</sub> and the Mg-rich matrix. For Case-II, the measured average hardness of the CP-Al and AA6061 coatings are 48.2 and 72.8 HV, respectively. As expected, the CP-Al layer is significantly softer than the underlying AZ91 substrate or the AA6061 layer.

Fig. 11 shows the wear volume and wear rate of the Case-II coating compared to that of the uncoated AZ91 substrate, as well as

representative wear profiles obtained using an optical surface profilometer (Fig. 11(a)). Representative friction coefficient measurements as a function of experimental wear distance shows the coated sample to have a coefficient of friction  $0.4 \pm 0.1$  and the uncoated substrate to have a coefficient of friction value of  $0.2 \pm 0.02$  throughout the duration of the wear experiment. The higher standard deviation in the coefficient plot indicate the possibility of abrasive wear due to the wear debris generated in the coating. Both the wear volume and wear rate were observed to be greater in the case of the uncoated AZ91 substrates as compared to that of the Case II coated substrates (Fig. 11(b)). Interestingly, comparing the wear behavior of the cold spray coated AA6061 with that of wrought AA6061-T6 (representative wear rate =  $7.9 \times 10^{-4}$  mm<sup>3</sup>/N.m) shows that they possess similar wear properties. This indicates that coupling the Case-II cold sprayed AZ91 plate with a wrought AA6061 plate in service is possible.

Finally, adhesion strength of the coating was evaluated by performing adhesion tests according to ASTM D4541. Measured bond strengths are 17.4 and 16.7 MPa for Case-I and Case-II, respectively. Although the observed bond strength was similar in both the cases, a significant decrease in porosity was noticed in Case-II samples, which is beneficial in terms of improving corrosion properties. A cohesive failure mode was observed in deposits for both the coatings. This indicates that the strength of the interface is greater than the coating.

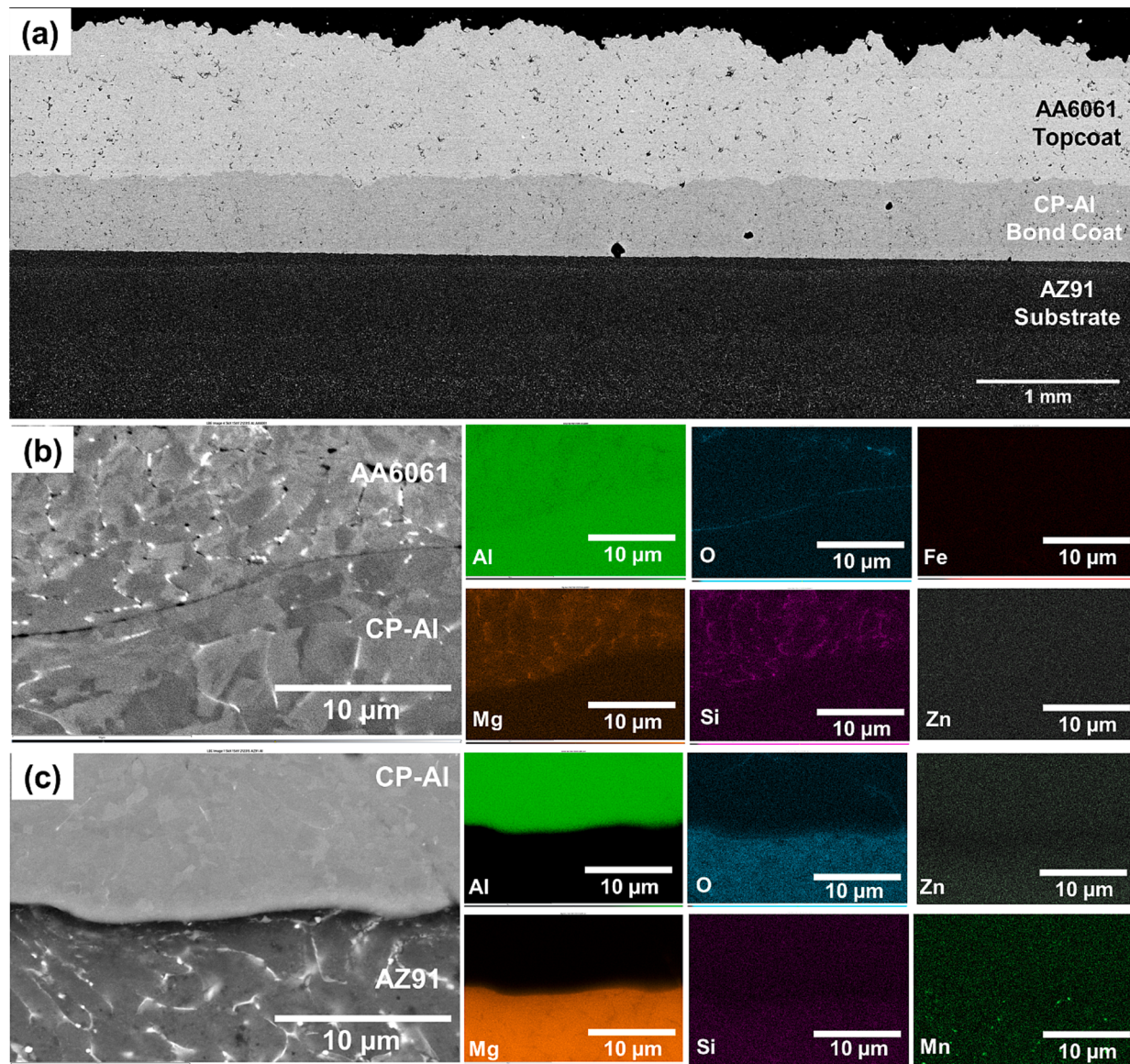


**Fig. 5.** SEM and EDS analysis of the cross section of a sample from Case-II. (a) Montage showing the deposited AA6061 coating and bond coat CP-Al coating on AZ91 substrate. (b) High-resolution micrographs of the AA6061 coating, AA6061/CP-Al interface, CP-Al layer coating, CP-Al/AZ91 interface, and AZ91 substrate. (c) High-resolution micrograph of the interface between the AA6061 and CP-Al coatings, and their corresponding EDS maps. (d) High-resolution micrograph of the interface between the CP-Al coating and AZ91 substrate, and their corresponding EDS maps.

**Table 3**  
Coating roughness, porosity and roughness of coatings.

	Thickness (μm)	Porosity (%)	Max. Surface roughness (μm)	Max. Substrate- Coating roughness (μm)
Case-I	398 ± 153	AA6061: 1.77	594 ± 3	66 ± 3
Case- II	962 ± 81	CP-Al: 0.34	294 ± 3	Substrate- CP-Al: 18 ± 3
		AA6061: 0.41		CP-Al - AA6061: 143 ± 3

### 3.4. Corrosion performance

#### 3.4.1. Multimodal macroscopic corrosion measurement

A comparison was made between the accelerated corrosion performance of uncoated AZ91, AZ91 coated with Case I parameters (i.e., just AA6061 coating) and Case II parameters (i.e., bond coat of CP-Al and top

coat of AA6061). We employed a newly designed multimodal corrosion measurement system to perform accelerated corrosion testing on these samples. The measurements involve performing OCP estimation for a duration of 1,800 s, followed by PD measurement. Simultaneously, the sample was imaged during the entirety of the corrosion duration. Fig. 12 shows an example of accelerated corrosion performed on the Case-II sample with both the bond and top coatings. Red circular annotations on the OCP and PD curves point to locations where snippet images of the corroding sample are shown below. The lack of corrosion attacks on the surface until the  $E_{corr}$  (~−700 mV [vs. SCE]) indicates that the coating is uniform and protects the AZ91 surface. This is indicated by the absence of evolving hydrogen ( $H_2$ ) bubbles on the surface, which is an excellent indicator of local and global corrosion progress in light metal alloys [32,38]. Until the start of the anodic polarization curve (approximately −700 mV [vs. SCE]), the sample surface is intact and does not undergo any corrosion attack (Fig. 12(a), 12(b) and 12(c)). This potential is significantly more noble compared to the  $E_{corr}$  of AZ91. However, on increasing the applied potential into the anodic regime of AA6061,

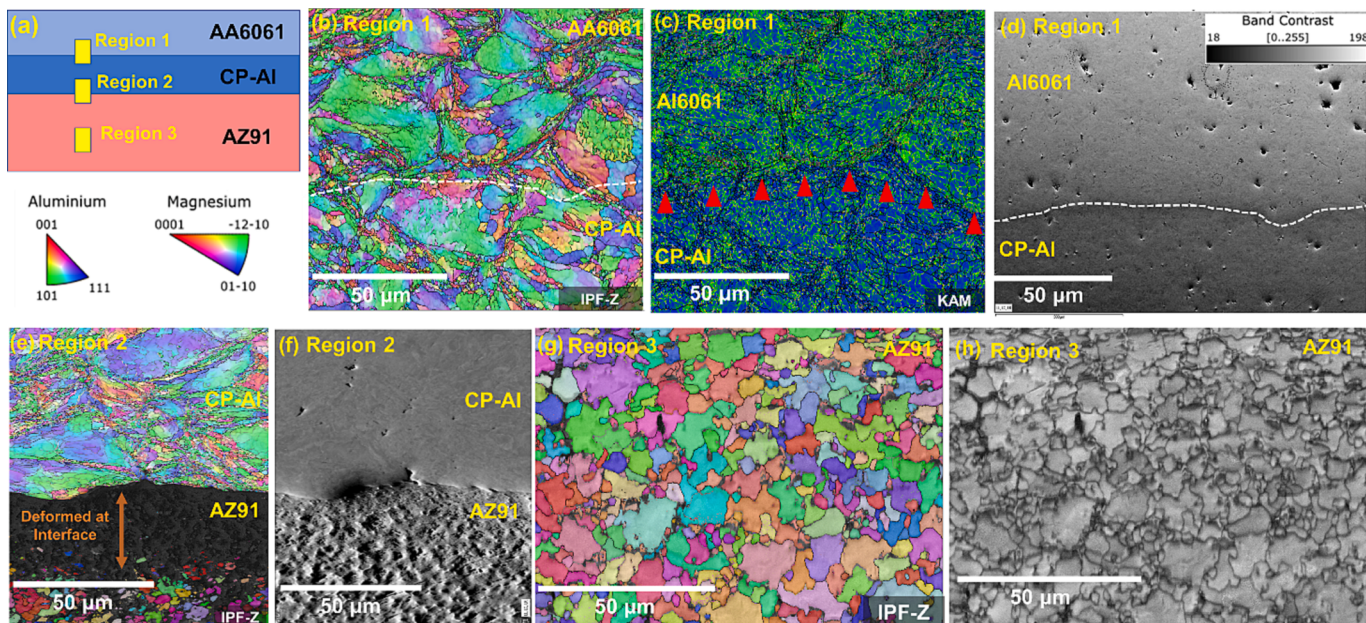


**Fig. 6.** (a) Schematic showing the cross section of a sample from Case II and locations of three regions where EBSD analysis was performed. (b) (c) (d): EBSD, KAM, and band-contrast (BC) maps from region 1: AA6061- CP-Al interface. (e)(f): EBSD and BC map from region 2: CP-Al – substrate interface. (g)(h): EBSD and BC map from within the substrate.

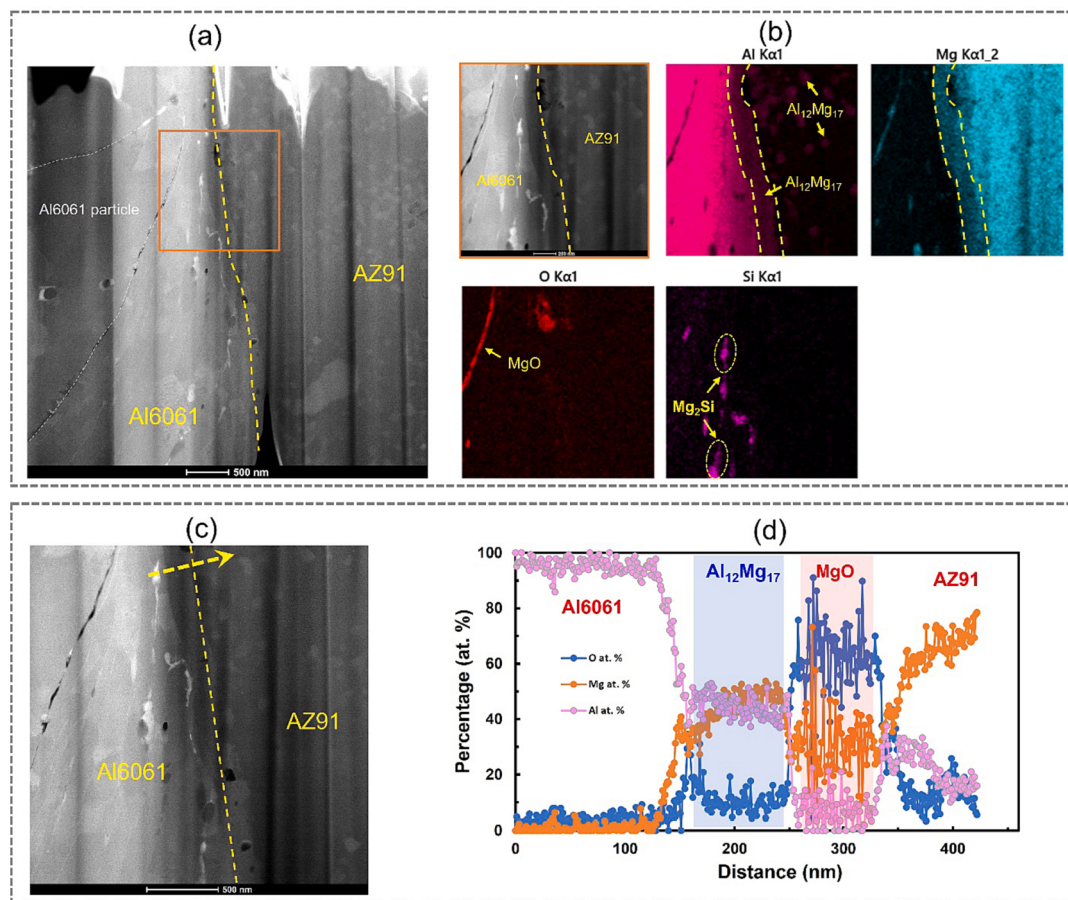


**Fig. 7.** Case I, (a) STEM image of AZ91-Al601 interface region. (b) EDS maps of Al, Mg, oxygen, Si, and Zn elemental distributions across the interface between substrate and coating. (c, d) EDS line scan across the Mg-Al interface (indicated by the arrow).

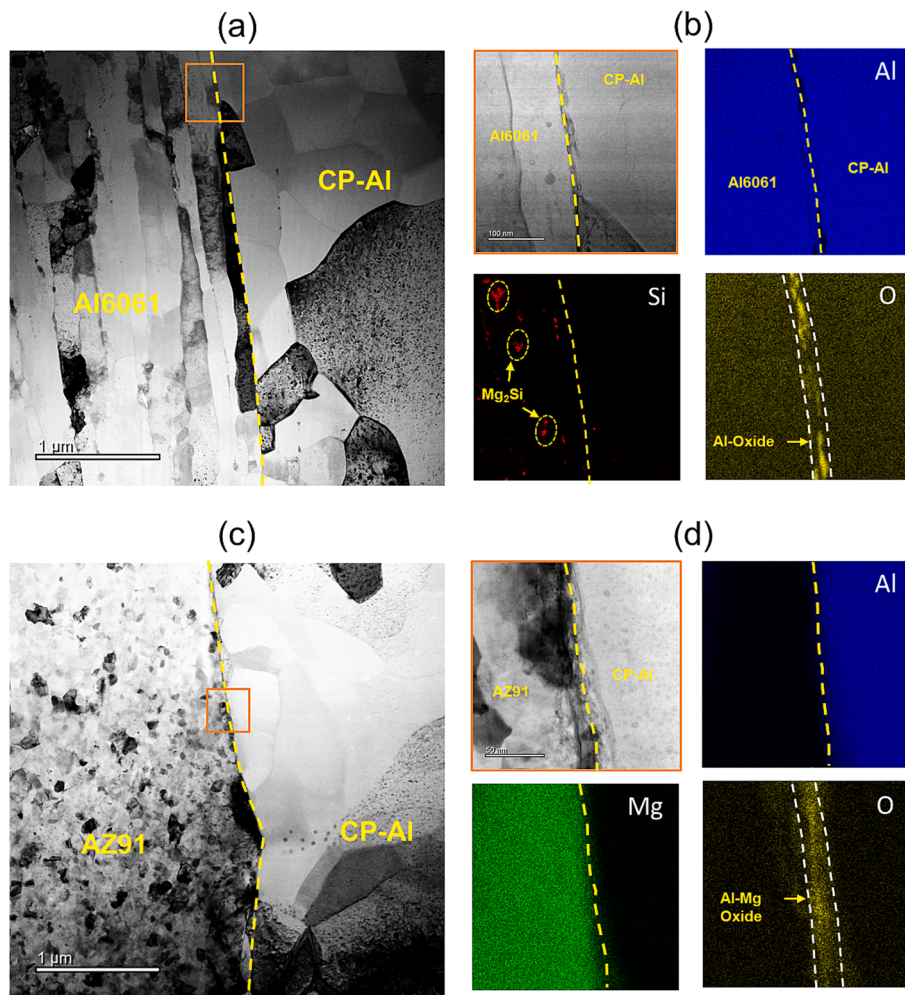
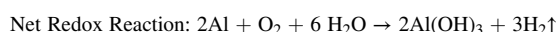
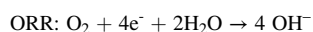
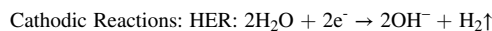


**Fig. 8.** (a) TEM bright field image showing AA6061 and CP-Al interface. (b) EDS area scan showing the AA6061-CP-Al interface with the elemental distribution of Al, Si, and oxygen. (c) Bright field image of the CP-Al and AZ91 interface. (d) EDS area scan of CP-Al-AZ91 interface region showing the elemental distribution of Al, Mg and oxygen.

localized corrosion is observed in the form of pitting, and  $\text{Al}^{3+}$  formation is accompanied by  $\text{H}_2$  release (Fig. 12(d)). With further increases in the applied anodic overpotential, the  $\text{H}_2$  bubble release rate as well as the overall volume of  $\text{H}_2$  released increased due to continued surface pitting corrosion that corresponds to potentials nobler than  $-300$  mV (Fig. 12(e)). The anodic and cathodic half reactions that accompany this release are shown below.



A contrasting corrosion behavior is evident by the sample from Case-I as shown in Fig. 13. Immediately upon immersing the sample into the 3.5 wt% NaCl solution (i.e., from the beginning of the OCP plot),  $\text{H}_2$  bubbles cover the entirety of the sample's surface, indicating that localized corrosion has already started during the OCP measurement (Fig. 13(a)). Such bubble release was observed to continue all throughout the OCP measurement and was characterized by the formation of a variety of  $\text{H}_2$  bubble sizes (up to 500  $\mu\text{m}$  in diameter) on the sample surface. This indicates that the rate of corrosion while consistent and ongoing, is different at different locations of the sample. That is, regions with larger and more stable bubbles show slower localized

corrosion and vice versa (Fig. 13(b)). At the start of the cathodic polarization curve from approximately  $-1600$  mV (vs. SCE), extensive bubble formation and release is observed on the surface as shown in Fig. 13(c).

Furthermore, this release of  $\text{H}_2$  continues until  $E_{\text{corr}}$  is reached ( $-1300$  mV (vs. SCE)). Note that this  $E_{\text{corr}}$  value does not correspond to the  $E_{\text{corr}}$  values of AA6061 (approximately  $-700$  mV (vs. SCE) [32]) or AZ91 (approximately  $-1600$  mV (vs. SCE) [32]). The rate of  $\text{H}_2$  bubble release once again slows significantly upon reaching  $E_{\text{corr}}$ , and the surface remains inactive until approximately  $-900$  mV (vs. SCE) (Fig. 13(d)). At this potential,  $\text{H}_2$  release once again resumes and increases rapidly until significant pitting is resolvable on the surface (Fig. 13(e)). Upon further increase in anodic overpotential, the sample continued to corrode with extensive  $\text{H}_2$  bubble release (Fig. 13(f)).

Finally, Fig. 14 shows the corrosion behavior of baseline AZ91. At the start of OCP, a small number of bubbles adhere to the surface. These bubbles marginally grow in size during the course of the OCP measurement (Fig. 14(a) and (b)). During the cathodic polarization process, more such bubbles form and grow in volume, covering the entire surface until  $E_{\text{corr}}$  is reached ( $-1480$  mV (vs. SCE)) (Fig. 14(c)). Upon entering the anodic polarization curve, small and rapid  $\text{H}_2$  bubble release is observed at different regions of the sample, signaling rapid localized corrosion attack ( $-1450$  mV (vs. SCE)) (Fig. 14(d)). As expected, the volume of  $\text{H}_2$  bubbles increases significantly with increased in applied overpotential (Fig. 14(e)). This process also is accompanied by

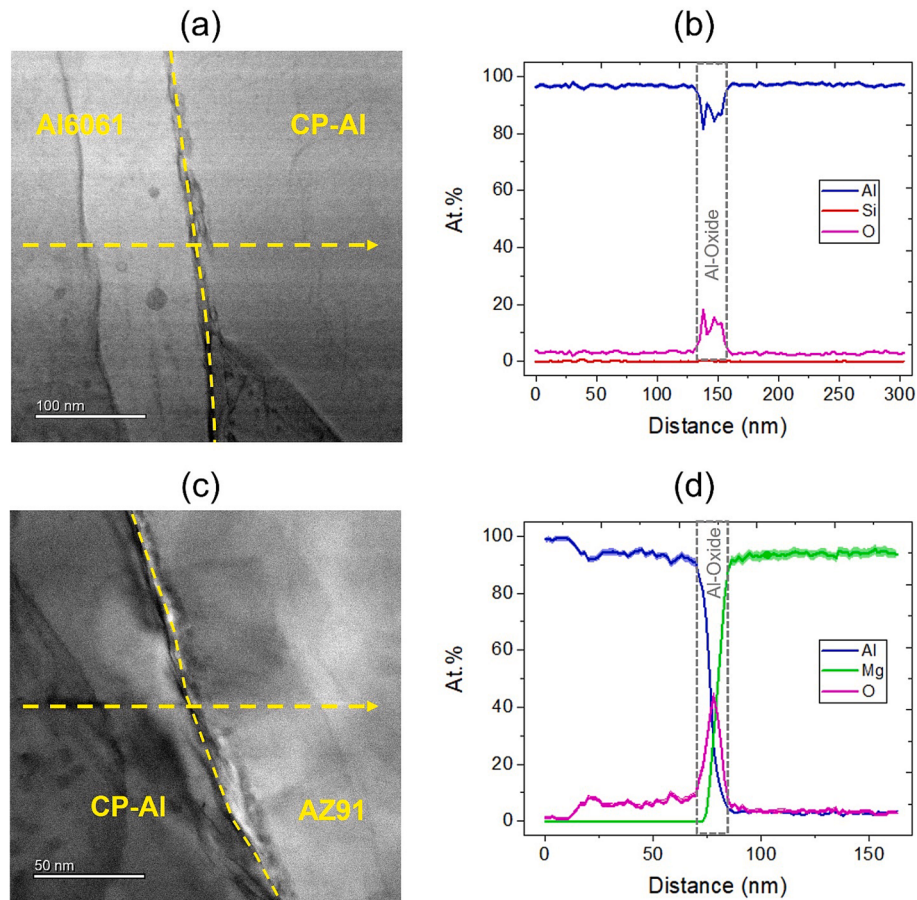


**Fig. 9.** TEM EDS line scan across the interface of (a, b) AA6061 coating-CP-Al bondcoat and (c, d) CP-Al bond coat-AZ91 substrate.

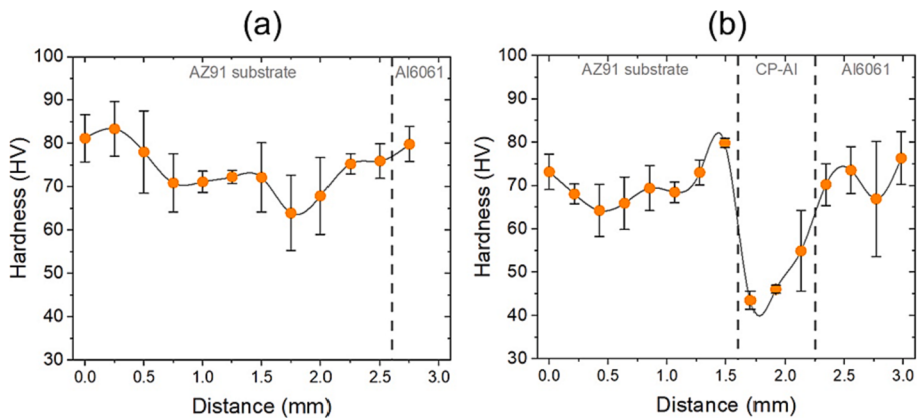
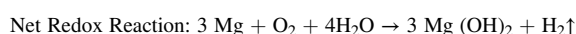
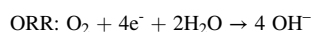
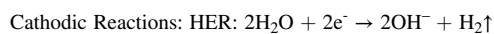
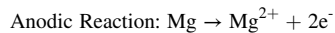


**Fig. 10.** Vickers microhardness of substrate and coatings of (a) Case-I and (b) Case -II samples.

significant surface pitting. The reactions involved during the corrosion of Mg are as follows [39]:



#### 3.4.2. Scanning electrochemical cell microscopy (SECCM)

SECCM was conducted locally within the coating and substrate regions of the sample. Because of the localized nature of this electrochemical technique, the substrate and the coating could be isolated so their individual electrochemical properties can be obtained. Fig. 15 shows Nyquist plots of the top coat (AA6061) and the substrate (AZ91). The equivalent circuit used to fit these Nyquist plots are shown in the inset of Fig. 15. The fitting parameter's solution resistance ( $R_s$ ), charge transfer resistance ( $R_{ct}$ ), double layer capacitance ( $C_{dl}$ ), diffusion/Warburg impedance ( $Z_w$ ) and goodness of fit are obtained from fitting curves and are shown in Table 4. The resistance, in particular the  $R_{ct}$  or the charge transfer resistance shows that the surface of the coating is ~

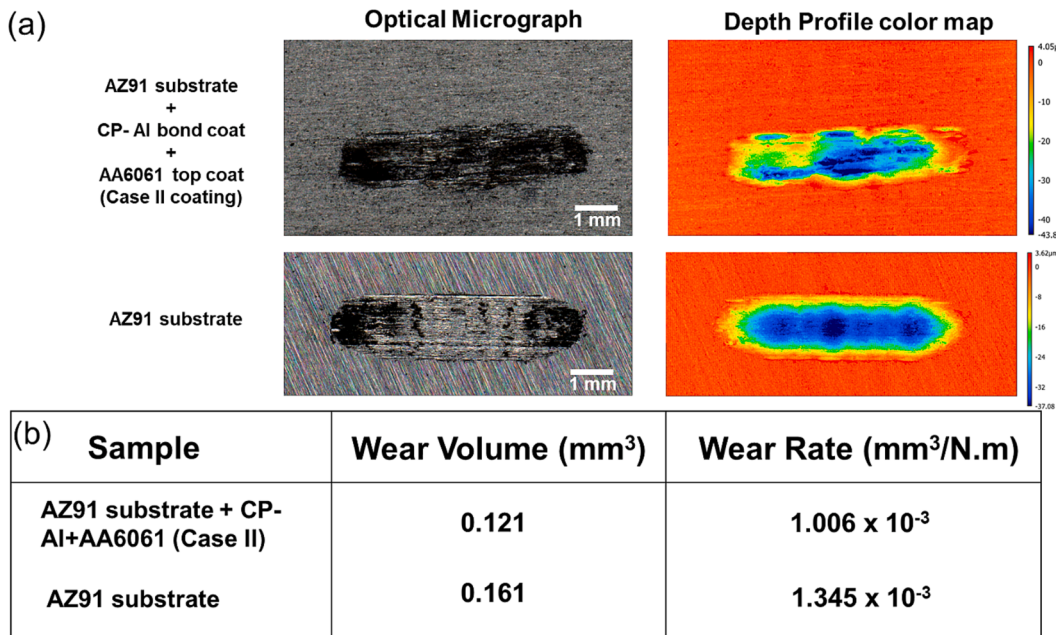


**Fig. 11.** (a) Optical and depth profiles of representative wear tracks and (b) table showing representative wear volumes and wear rates for case II coating and uncoated AZ91 sample.

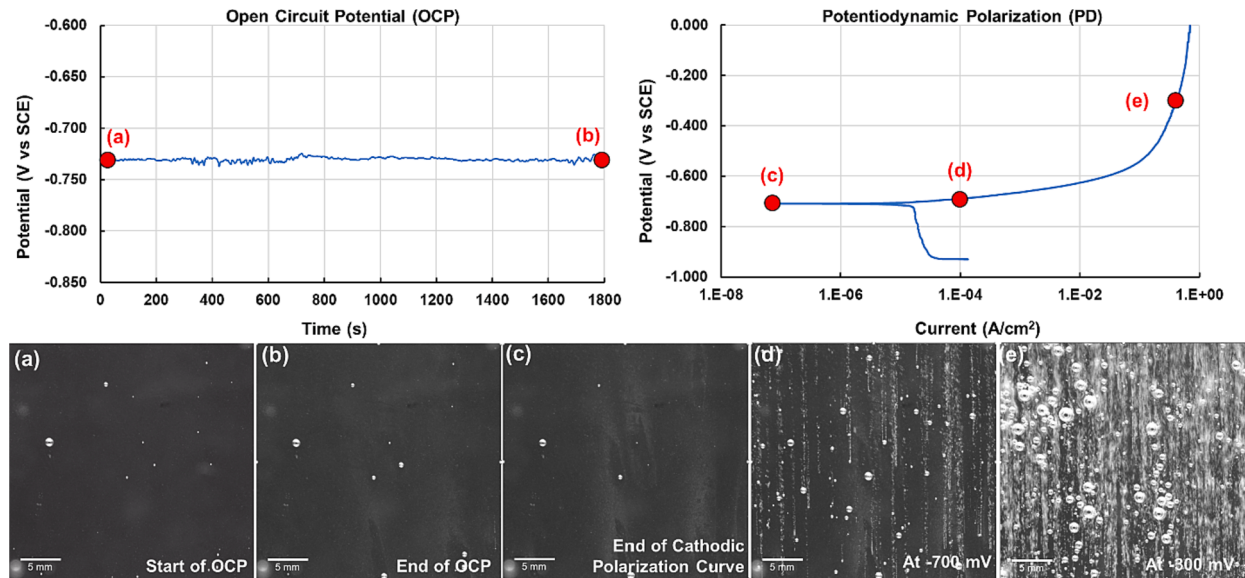


**Fig. 12.** OCP vs. time and Potentiodynamic polarization plot for Case II coating. Regions of the plots from where snippet images of the corroding surface are also depicted.

2.3 times greater than that of the substrate. This indicates that the coating is inherently more resistant to corrosion attack in salt water conditions.

#### 4. Discussion

This study describes the microstructure and performance of three cases: uncoated AZ91, AA6061 cold spray coated AZ91, and AZ91 cold spray coated with CP-Al as a bond coat and AA6061 as top coat. Micrographs, EDS results, and EBSD results of the cases/conditions discussed in this manuscript show a substantial improvement in coating deposition, uniformity of coating, roughness of coating and a significant decrease in porosity in the Case-II coating compared to the Case-I coating.

For implementation in automotive applications and joining/contact with other Al alloys, the corrosion and mechanical properties of the coating are critical. Hardness results indicate that the CP-Al is softer than AZ91. The soft Al layer is also more uniform and has a lower roughness compared to the AZ91 substrate and thus facilitates the deposition of the AA6061 powders. Furthermore, mechanical testing results indicate a notable improvement in wear behavior. The coating exhibits a promising adhesion strength that can be improved using appropriate heat treatment to enhance diffusion at the interface. The Case-II coating also shows excellent corrosion performance as compared to the Case-I coating or the uncoated AZ91. As is evident from the OCP and PD behaviors, the corrosion process is similar to that of the wrought AA6061, as shown by its PD plot included in Fig. 16 [32]. Furthermore, the uncoated AZ91 has an  $E_{corr}$  value  $\sim 900$  mV lower than that of Case-

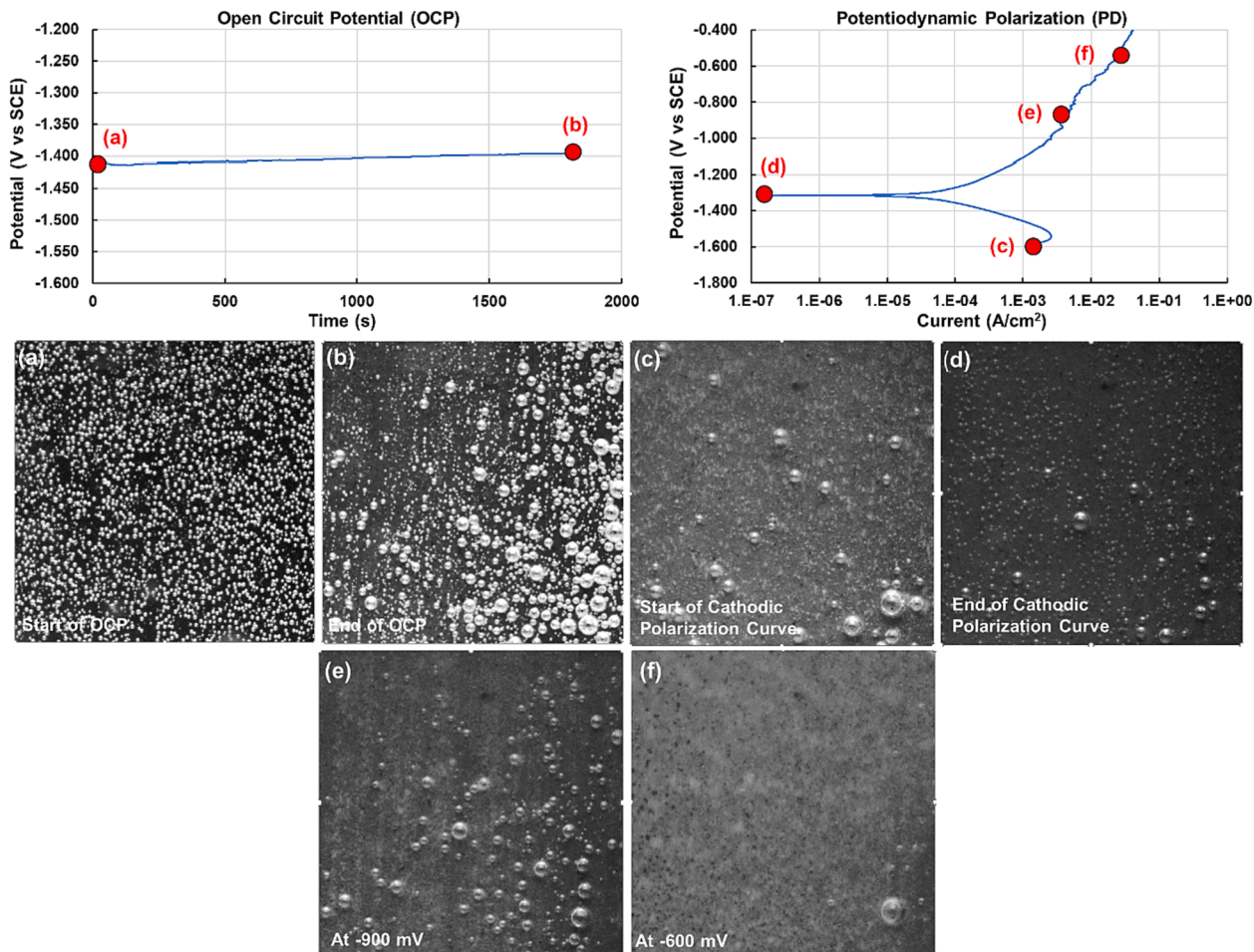


**Fig. 13.** Open circuit potential (OCP) vs time and Potentiodynamic polarization plot for Case II coating. Regions of the plots from where snippet images of the corroding surface are also depicted.

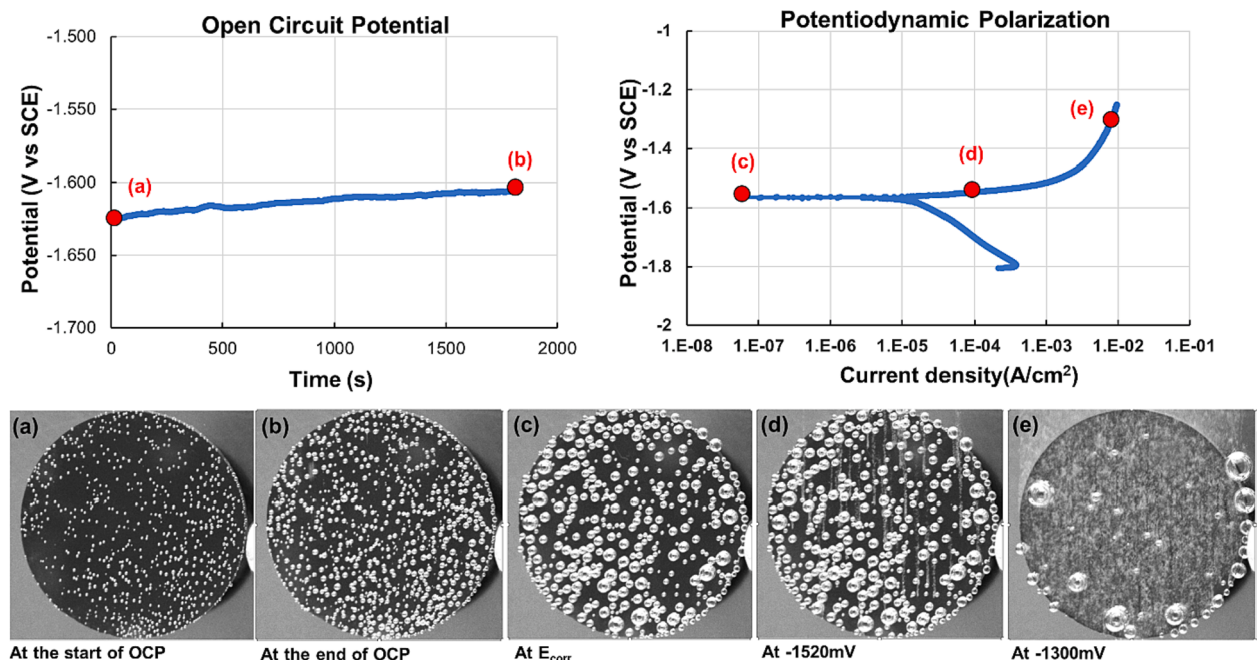


**Fig. 14.** OCP vs. time and PD polarization plots for pristine AZ91, which is the baseline for comparison. Regions of the plots from where snippet images of the corroding surface were taken also are depicted. (a) At the start of the OCP measurement, (b) At the end of the OCP measurement, (c) At  $E_{corr}$ , (d) At  $-1520\text{ mV}$  ( $\text{V vs SCE}$ ) and (e) At  $-1300\text{ mV}$  ( $\text{V vs SCE}$ ).

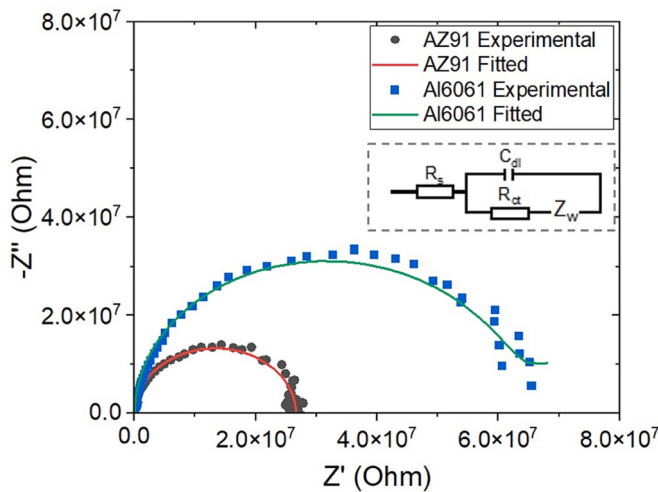


**Fig. 15.** Nyquist plots comparing the impedance behavior between AZ91 (grey) and AA6061 (blue). The experimental Nyquist curves are fitted using an equivalent circuit diagram as shown. Symbols indicate the experimental data and solid lines indicate the fitting data. (For interpretation of the references to colour in this figure legend, the reader is referred to the web version of this article.)

**Table 4**

Fitted data from electrochemical impedance spectroscopy of AZ91 substrate and Al6061 coating.

Material	$R_s$ (Ohm)	$C_{dl}$ (F)	$R_{ct}$ (Ohm)	$Z_w$ (Ohm $s^{-1/2}$ )	$\chi^2/ Z $
AZ91	73.9	$23.9 \times 10^{-12}$	$26.5 \times 10^6$	$12.7 \times 10^6$	0.46
Al6061	78.9	$25.6 \times 10^{-12}$	$60.8 \times 10^6$	$35.8 \times 10^6$	0.56

II coating. This indicates a significant improvement in the readiness to corrode under a corrosive saline environment.

Interestingly, Case-I showed corrosion performance unlike the uncoated AZ91, and the Case-II AA6061 coated AZ91. The added imaging modality aids significantly in deducing the possible mechanism associated with the corrosion of this sample. The schematic shown in Fig. 17 summarizes the mechanism of corrosion attack in Case -I (Fig. 17(a)) and Case-II (Fig. 17(b)) samples.

The Case-I coating is characterized by the presence of a very discontinuous, non-uniform, and porous coating. The substrate potentially is exposed in several regions of the coated surface. Immediately upon immersion into the 3.5 wt% NaCl solution, the exposed AZ91 begins to corrode accompanied by significant H<sub>2</sub> bubble release. This is followed by the formation of Mg(OH)<sub>2</sub> that covers the exposed areas thereby rendering the sample nearly inert to corrosion from the E<sub>corr</sub> of the sample up to approximately -900 mV. Above approximately -900 mV, the AA6061 coating begins to undergo corrosion and releases significant quantities of H<sub>2</sub>. We hypothesize that this release is also accompanied by the removal of Mg(OH)<sub>2</sub>, which leads to both the AZ91 and AA6061 being corroded in the sample. Thus, the performance of the Case-I coating is compromised severely due to the uneven deposition of the coating. Such a behavior was not observed in the coatings in Case-II, which performed similarly to wrought AA6061 as no substrate is exposed and also due to significantly lower porosity.

## 5. Conclusions

CP-Al cold sprayed bond coatings were used to enable the deposition of AA6061 powders on AZ91 coupons. These coatings (Case-II) were compared with the case where only the AA6061 powders were deposited on the substrate using the same parameters (Case-I), and with the uncoated AZ91 substrate. Coating performance was evaluated using several mechanical and corrosion measurement tools to evaluate the coatings for automotive applications. Our results indicate:

- The use of soft CP-Al powder bond coating enables deposition of AA6061 powders better than AA6061 powders could deposit on the AZ91 substrate by itself. Additionally, these bilayer coatings (Case-II) exhibit very low porosity as compared to Case-I coating.
- The CP-Al bond coat forms a more uniform, less porous layer on the AZ91 substrate compared to AA6061 due increased deformation. The uniform bond coat reduces surface roughness and porosity which creates a surface conducive for the deposition of AA6061 coating.
- Mechanical performance of the coating was notably better than the uncoated substrate. While the hardness of AA6061 remained similar to AZ91 (and similar to the hardness of solutionized condition of wrought AA6061), the wear rate of the coating was at least 25 % lower than that of the uncoated substrate.
- The corrosion properties of the optimized coating were substantially better as compared to that of the substrate. The E<sub>corr</sub> value of Case II

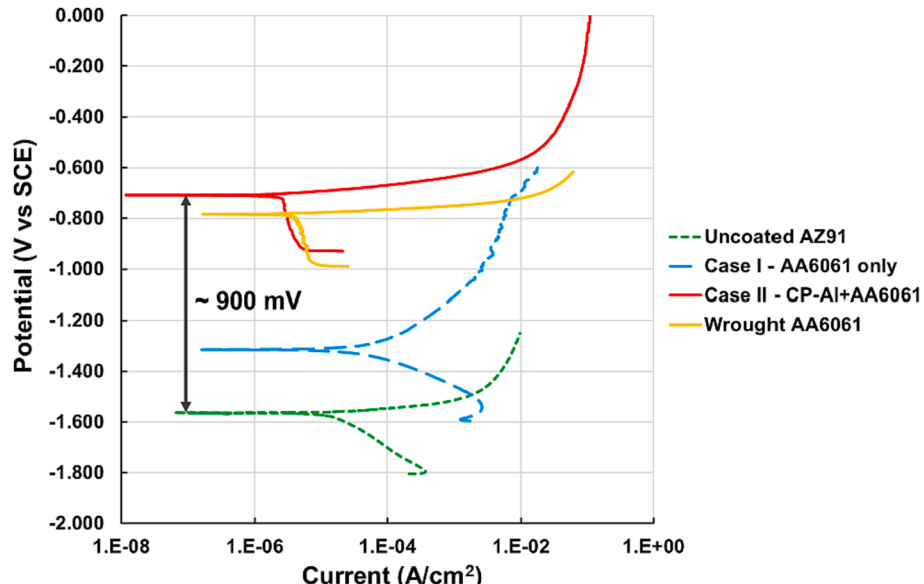


**Fig. 16.** Plot showing the potentiodynamic polarization behavior of uncoated AZ91, Case-I coated AZ91, Case-II coated AZ91 and wrought AA6061 for comparison.

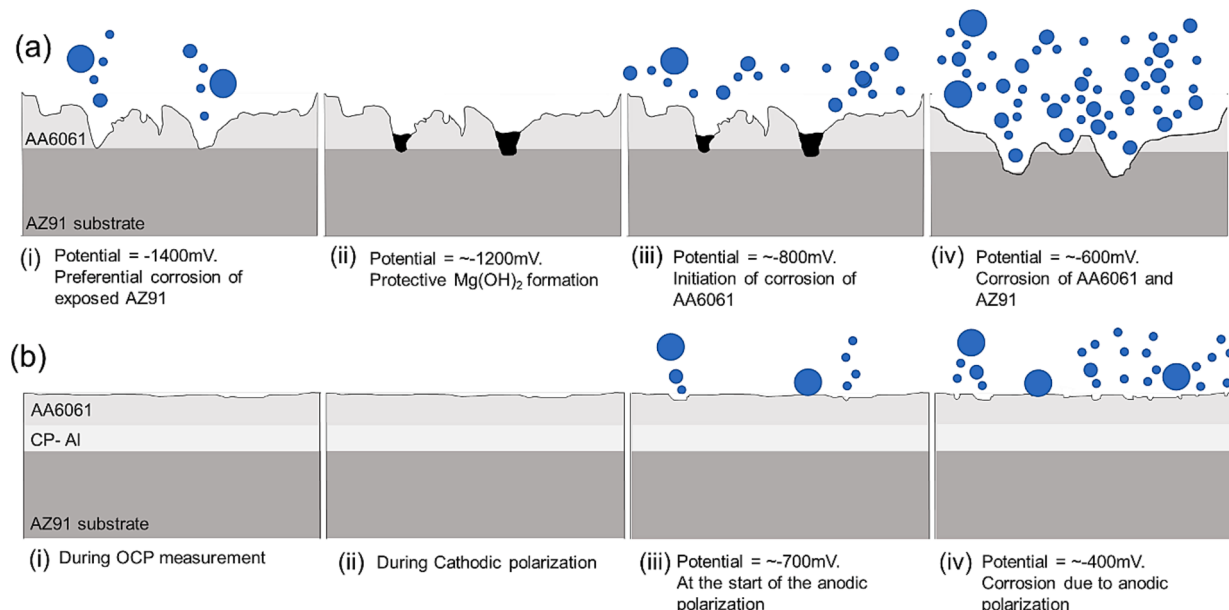


**Fig. 17.** Schematics showing the progress of corrosion attack. (a) Sample from Case-I wherein regions of the substrate are exposed. (i) The exposed AZ91 begins corroding first, accompanied by  $H_2$  bubble release, (ii) The exposed AZ91 forms a protective corrosion product comprising  $Mg(OH)_2$ , (iii) With increases in potential, the AA6061 coating begins to undergo corrosion, leading to rapid  $H_2$  bubble release, (iv) This release also exposes regions covered with  $Mg(OH)_2$  and thereby, due to the high positive value of the imposed anodic overpotential, both the AZ91 and AA6061 continue to corrode until stopped. (b) Sample from Case-II wherein a bond coating and top coating are used, (i) and (ii) The coatings and the substrate are undisturbed during the open circuit measurement, (iii) At the start of the anodic polarization, localized  $H_2$  bubble release in the form of trickles of  $H_2$  bubble release from corroding sites on the surface, (iv) At approximately  $-400$  mV, severe  $H_2$  bubble release is seen and signs of pitting also are visible on the surface. However, no AZ91 substrate is exposed due to the slow rate of coating degradation and the thickness of the coating.

coating was 900 mV more noble compared to the AZ91 substrate. Electrochemical impedance spectroscopy measurements obtained using SECCM showed a greater than 2X increase in the resistance to corrosion in the Case-II coatings as compared to the substrate.

These performance metrics indicate that the Case II coating notably improves the surface properties of the AZ91 Mg alloy. Additionally, cold spray instrumentation can easily be integrated into existing automotive manufacturing lines using robotic arms. Furthermore, these coatings are comprised of materials that are already used by the automotive industry; therefore, they would place no extra burden on the automotive or end-of-life recycling pipelines.

#### CRediT authorship contribution statement

**Sridhar Niverty:** Conceptualization, Formal analysis, Investigation, Methodology, Software, Validation, Visualization, Writing – original draft. **Rajib Kalsar:** Conceptualization, Formal analysis, Investigation, Methodology, Software, Validation, Visualization, Writing – review & editing. **Anthony J. Naccarelli:** Formal analysis, Methodology, Resources, Writing – original draft. **Timothy J. Eden:** Project administration, Resources, Writing – review & editing. **Xiaolong Ma:** Carrying out measurements and manuscript composition. **Nicole Overman:** Investigation, Methodology, Resources, Software. **Glenn Grant:** Funding acquisition, Project administration, Resources, Supervision. **Darrell Herling:** Funding acquisition, Project administration, Resources, Supervision. **Vineet V. Joshi:** Conceptualization, Experimental design, Manuscript composition, Project administration, Resources, Supervision, Funding acquisition.

#### Declaration of competing interest

The authors declare that they have no known competing financial interests or personal relationships that could have appeared to influence

the work reported in this paper.

#### Data availability

Data will be made available on request.

#### Acknowledgements

The authors acknowledge the support of the U.S. Department of Energy Vehicle Technologies Office. The authors are grateful to Daniel Graff and Gary G Neuenschwander in assisting with cold spray coatings and Anthony Guzman for metallurgical sample preparation. Pacific Northwest National Laboratory is operated by the Battelle Memorial Institute for the United States Department of Energy under contract DE-AC06-76LO1830.

#### Appendix A. Supplementary data

Supplementary data to this article can be found online at <https://doi.org/10.1016/j.matdes.2023.112579>.

#### References

- [1] DOE-EERE, Lightweight Technologies for Cars and Trucks- Vehicle Technologies Office, (n.d.). <https://www.energy.gov/eere/vehicles/lightweight-materials-cars-and-trucks>.
- [2] K.U. Kainer, *Magnesium – alloys and technology*, Wiley & Sons Inc, 2003.
- [3] M. Esmaily, J.E. Svensson, S. Fajardo, N. Birbilis, G.S. Frankel, S. Virtanen, R. Arrabal, S. Thomas, L.G. Johansson, Fundamentals and advances in magnesium alloy corrosion, *Prog. Mater. Sci.* 89 (2017) 92–193, <https://doi.org/10.1016/j.pmatsci.2017.04.011>.
- [4] J.P. Weiler, G. Wang, R. Berkmarcel, Assessment of cyclic corrosion test protocols for magnesium substrates, *SAE Int. J. Mater. Manuf.* 11 (2018) 481–490, <https://doi.org/10.4271/2018-01-0103>.
- [5] W.J. Joost, P.E. Krajewski, Towards magnesium alloys for high-volume automotive applications, *Scr. Mater.* 128 (2017) 107–112, <https://doi.org/10.1016/j.scriptamat.2016.07.035>.

- [6] S. Fleming, An Overview of Magnesium based Alloys for Aerospace and Automotive Applications by, (2012) 1–36.
- [7] P. Predko, D. Rajnovic, M.L. Grilli, B.O. Postolnyi, V. Zemcenkovs, G. Rijkuris, E. Pole, M. Lissanskis, Promising methods for corrosion protection of magnesium alloys in the case of mg-al, mg-mn-ce and mg-zn-zr: A recent progress review, *Metals* (Basel) 11 (2021), <https://doi.org/10.3390/met11071133>.
- [8] K. Lazarz, J. Cahill, T.J. Ciccone, K. Redlin, S. Simko, Corrosion Performance of a Magnesium Tower Brace, *SAE Tech. Pap.* (2021) 1–7. 10.4271/2021-01-0276.
- [9] R.C. McCune, J. Forsmark, B. Schneider, A. Luo, H. Gu, W. Schumacher, X. Chen, F. Vartolas, Development of corrosion testing protocols for magnesium alloys and magnesium-intensive subassemblies, *SAE Int. J. Mater. Manuf.* 6 (2013) 242–247, <https://doi.org/10.4271/2013-01-0978>.
- [10] B. Marzbanrad, E. Toyserkani, H. Jahed, Customization of residual stress induced in cold spray printing, *J. Mater. Process. Tech.* 289 (2021), <https://doi.org/10.1016/j.jmatprotec.2020.116928>.
- [11] E. Irissoou, J.-G. Legoux, A.N. Ryabinin, B. Jodoin, C. Moreau, Review on Cold Spray Process and Technology: Part I-Intellectual Property, (n.d.). 10.1007/s11666-008-9203-3.
- [12] S.M. Hassani-Gangaraj, A. Moridi, M. Guagliano, Critical review of corrosion protection by cold spray coatings, *Surf. Eng.* 31 (2015) 803–815, <https://doi.org/10.1179/1743294415Y.0000000018>.
- [13] A. Moridi, S.M. Hassani-Gangaraj, M. Guagliano, M. Dao, Cold spray coating: Review of material systems and future perspectives, *Surf. Eng.* 30 (2014) 369–395, <https://doi.org/10.1179/1743294414Y.0000000270>.
- [14] V.C. Jr, N. Matthews, V.C. Iii, Introduction to Supersonic Particle Deposition, Elsevier Ltd. (2018), <https://doi.org/10.1016/B978-0-08-100540-8.00014-5>.
- [15] K. Spencer, M.X. Zhang, Heat treatment of cold spray coatings to form protective intermetallic layers, *Scr. Mater.* 61 (2009) 44–47, <https://doi.org/10.1016/j.scriptamat.2009.03.002>.
- [16] K. Spencer, D.M. Fabijanic, M.X. Zhang, The use of Al-Al<sub>2</sub>O<sub>3</sub> cold spray coatings to improve the surface properties of magnesium alloys, *Surf. Coatings Technol.* 204 (2009) 336–344, <https://doi.org/10.1016/j.surfcoat.2009.07.032>.
- [17] Q. Wang, K. Spencer, N. Birbilis, M.X. Zhang, The influence of ceramic particles on bond strength of cold spray composite coatings on AZ91 alloy substrate, *Surf. Coatings Technol.* 205 (2010) 50–56, <https://doi.org/10.1016/j.surfcoat.2010.06.008>.
- [18] Q. Wang, N. Birbilis, M.X. Zhang, Process optimisation of cold spray Al coating on AZ91 alloy, *Surf. Eng.* 30 (2014) 323–328, <https://doi.org/10.1179/1743294413Y.0000000224>.
- [19] Y.K. Wei, X.T. Luo, Y. Ge, X. Chu, G.S. Huang, C.J. Li, Deposition of fully dense Al-based coatings via in-situ micro-forging assisted cold spray for excellent corrosion protection of AZ31B magnesium alloy, *J. Alloys Compd.* 806 (2019) 1116–1126, <https://doi.org/10.1016/J.JALLCOM.2019.07.279>.
- [20] Y. Bai, Z.H. Wang, X.B. Li, G.S. Huang, C.X. Li, Y. Li, Corrosion behavior of low pressure cold sprayed Zn-Ni composite coatings, *J. Alloys Compd.* 719 (2017) 194–202, <https://doi.org/10.1016/J.JALLCOM.2017.05.134>.
- [21] T. Schmidt, H. Assadi, F. Gärtnner, H. Richter, T. Stoltenhoff, H. Kreye, T. Klassen, From Particle Acceleration to Impact and Bonding in Cold Spraying, *J. Therm. Spray Technol.* 2009 185. 18 (2009) 794–808. 10.1007/S11666-009-9357-7.
- [22] T. Schmidt, F. Gärtnner, H. Assadi, H. Kreye, Development of a generalized parameter window for cold spray deposition, (2005). 10.1016/j.actamat.2005.10.005.
- [23] S. Niverty, R. Kalsar, A. Naccarelli, T. Eden, G. Grant, V. Joshi, Optimization of the Microstructure and Performance of Aluminum Alloy Cold Spray Coatings on Magnesium Alloy Substrates, (2023) 49–51. 10.1007/978-3-031-22645-8\_12/ COVER.
- [24] Y. Tao, T. Xiong, C. Sun, L. Kong, X. Cui, T. Li, G.L. Song, Microstructure and corrosion performance of a cold sprayed aluminium coating on AZ91D magnesium alloy, *Corros. Sci.* 52 (2010) 3191–3197, <https://doi.org/10.1016/j.corsci.2010.05.023>.
- [25] A. Wank, B. Wielage, H. Podlesak, T. Grund, High-resolution microstructural investigations of interfaces between light metal alloy substrates and cold gas-sprayed coatings, *J. Therm. Spray Technol.* 15 (2006) 280–283, <https://doi.org/10.1361/105996306X108291>.
- [26] B. Marzbanrad, H. Jahed, E. Toyserkani, On the evolution of substrate's residual stress during cold spray process: A parametric study, *Mater. Des.* 138 (2018) 90–102, <https://doi.org/10.1016/J.MATDES.2017.10.062>.
- [27] B. Marzbanrad, M.H. Razmipoosh, E. Toyserkani, H. Jahed, Role of heat balance on the microstructure evolution of cold spray coated AZ31B with AA7075, *J. Magnes. Alloy.* 9 (2021) 1458–1469, <https://doi.org/10.1016/J.JMA.2021.03.009>.
- [28] S. Niverty, R. Kalsar, L. Strange, V. Prabhakaran, V. V. Joshi, Integrating Multimodal Corrosion with Correlative Microscopy Across Multiple Length Scales, (2023) 63–64. 10.1007/978-3-031-22645-8\_15/COVER.
- [29] L.C. Yule, C.L. Bentley, G. West, B.A. Shollock, P.R. Unwin, Scanning electrochemical cell microscopy: A versatile method for highly localised corrosion related measurements on metal surfaces, *Electrochim. Acta.* 298 (2019) 80–88, <https://doi.org/10.1016/J.ELECTACTA.2018.12.054>.
- [30] V. Prabhakaran, R. Kalsar, L. Strange, O.A. Marina, R. Prabhakaran, V.V. Joshi, Understanding Localized Corrosion on Metal Surfaces Using Scanning Electrochemical Cell Impedance Microscopy (SECCIM), *J. Phys. Chem. C.* 126 (2022) 12519–12526, [https://doi.org/10.1021/ACS.JPCC.2C03807/ASSET/IMAGES/LARGE/JP2C03807\\_0006.JPG](https://doi.org/10.1021/ACS.JPCC.2C03807/ASSET/IMAGES/LARGE/JP2C03807_0006.JPG).
- [31] H. Assadi, T. Schmidt, H. Richter, J.-O. Kliemann, K. Binder, F. Gärtnner, T. Klassen, H. Kreye, On Parameter Selection in Cold Spraying, (n.d.). 10.1007/s11666-011-9662-9.
- [32] S. Niverty, R. Kalsar, R.J. Seffens, A.D. Guzman, T.J. Roosendaal, L. Strange, V. V. Joshi, Probing corrosion using a simple and versatile in situ multimodal corrosion measurement system, *Sci. Rep.* 13 (2023) 16695, <https://doi.org/10.1038/s41598-023-42249-0>.
- [33] A.T. Ernst, P. Kerns, A. Nardi, H.D. Brody, A.M. Dongare, S.-W. Lee, V.K. Champagne, S.L. Suib, M. Aindow, Surface states of gas-atomized Al 6061 powders-Effects of heat treatment, (2020). 10.1016/j.apsusc.2020.147643.
- [34] S. Niverty, J. Sun, J. Williams, F. Bachmann, N. Gueninchault, E. Lauridsen, N. Chawla, A Forward Modeling Approach to High-Reliability Grain Mapping by Laboratory Diffraction Contrast Tomography (LabDCT), *JOM.* 71 (2019) 2695–2704, <https://doi.org/10.1007/s11837-019-03538-0>.
- [35] O. Lunder, J.E. Lein, T.K. Aune, K. Nisancioğlu, The Role of Mg17Al12 Phase in the Corrosion of Mg Alloy AZ91, *Corrosion.* 45 (1989) 741–748, <https://doi.org/10.5006/1.3585029>.
- [36] M.X. Zhang, P.M. Kelly, Crystallography of Mg17Al12 precipitates in AZ91D alloy, *Scr. Mater.* 48 (2003) 647–652, [https://doi.org/10.1016/S1359-6462\(02\)00555-9](https://doi.org/10.1016/S1359-6462(02)00555-9).
- [37] H. Bu, M. Yandouzi, C. Lu, B. Jodoin, Effect of heat treatment on the intermetallic layer of cold sprayed aluminum coatings on magnesium alloy, *Surf. Coatings Technol.* 205 (2011) 4665–4671, <https://doi.org/10.1016/j.surfcoat.2011.04.018>.
- [38] Y. Yang, F. Scenini, M. Curioni, A study on magnesium corrosion by real-time imaging and electrochemical methods: relationship between local processes and hydrogen evolution, *Electrochim. Acta.* 198 (2016) 174–184, <https://doi.org/10.1016/J.ELECTACTA.2016.03.043>.
- [39] G.S. Frankel, A. Samaniego, N. Birbilis, Evolution of hydrogen at dissolving magnesium surfaces, *Corros. Sci.* 70 (2013) 104–111, <https://doi.org/10.1016/J.CORSCL.2013.01.017>.